Research Article | Vol. 25, No. 23 | 13 Nov 2017 | OPTICS EXPRESS 29098
Optics EXPRESS

Unveiling multi-scale laser dynamics through time-stretch and time-lens spectroscopies

XIAOMING WEI,[1,5] BOWEN LI,[2,5] YING YU,[2,5] CHI ZHANG,[3,4] KEVIN K. TSIA,[2] AND KENNETH K. Y. WONG[2,*]

[1]*Present address: Division of Engineering and Applied Science, California Institute of Technology, 1200 East California Boulevard, Pasadena, CA 91125, USA*
[2]*Department of Electrical and Electronic Engineering, The University of Hong Kong, Pokfulam Road, Hong Kong, China*
[3]*Present address: Wuhan National Laboratory for Optoelectronics, Huazhong University of Science and Technology, Wuhan 430074, China*
[4]*chizheung@hust.edu.cn*
[5]*These authors contributed equally to this work.*
**kywong@eee.hku.hk*

Abstract: Spectro-temporal studies on the nonlinear physics of complex laser dynamics are essential in approaching its ultimate performance as well as understanding interdisciplinary problems. Unfortunately, it has long been limited by the insufficient spectro-temporal resolving power of conventional temporal and spectral analyzers, particularly when an indefinite optical signal ensemble contains polychromatic mixtures of continuous-wave (CW) and short pulse. In this work, we propose a real-time optical spectro-temporal analyzer (ROSTA) with three synchronized processing channels (i.e., multi-core) for single-shot studies on laser dynamics. It simultaneously provides temporal resolutions of ~70 ps in the time domain and 10's ns (or 10's MHz frame rate) in the spectral domain, as well as a high spectral resolution for multiscale optical inputs, i.e., ranging from CW to fs pulses. Its non-trivial record length of up to 6.4 ms enables continuous observations of non-repetitive optical events over an extensive time period — equivalent to a propagation distance of ~1900 km. To showcase its practical applications, ROSTA is applied to visualize the onset of passive mode-locking of a fiber laser, and interesting phenomena, i.e., evolution from quasi-CW noise burst to strong shock, transition from fluctuation to mode-locking, and coexistence of CW and mode-locked pulses, have been spectro-temporally observed in a single-shot manner for the first time. It is anticipated that ROSTA will be a powerful technology for spectro-temporal optical diagnosis in different areas involving polychromatic transients.

OCIS codes: (320.7140) Ultrafast processes in fibers; (140.4050) Mode-locked lasers; (190.7110) Ultrafast nonlinear optics; (300.6530) Spectroscopy, ultrafast.

References and links

1. M. H. Huang, S. Mao, H. Feick, H. Yan, Y. Wu, H. Kind, E. Weber, R. Russo, and P. Yang, "Room-temperature ultraviolet nanowire nanolasers," Science **292**(5523), 1897–1899 (2001).
2. D. J. Richardson, J. Nilsson, and W. A. Clarkson, "High power fiber lasers: current status and future perspectives (Invited)," J. Opt. Soc. Am. B **27**(11), B63–B92 (2010).
3. C. Jauregui, J. Limpert, and A. Tünnermann, "High-power fibre lasers," Nat. Photonics **7**(11), 861–867 (2013).
4. H. Rong, R. Jones, A. Liu, O. Cohen, D. Hak, A. Fang, and M. Paniccia, "A continuous-wave Raman silicon laser," Nature **433**(7027), 725–728 (2005).
5. M. E. Fermann and I. Hartl, "Ultrafast fibre lasers," Nat. Photonics **7**(11), 868 (2013).
6. G. P. Agrawal, Fiber-Optic Communication Systems, 3rd ed. (Wiley, New York, 2002).
7. L. Shah, A. Arai, S. Eaton, and P. Herman, "Waveguide writing in fused silica with a femtosecond fiber laser at 522 nm and 1 MHz repetition rate," Opt. Express **13**(6), 1999–2006 (2005).
8. R. R. Gattass and E. Mazur, "Femtosecond laser micromachining in transparent materials," Nat. Photonics **2**(4), 219–225 (2008).
9. T. Wilken, G. L. Curto, R. A. Probst, T. Steinmetz, A. Manescau, L. Pasquini, J. I. González Hernández, R. Rebolo, T. W. Hänsch, T. Udem, and R. Holzwarth, "A spectrograph for exoplanet observations calibrated at the centimetre-per-second level," Nature **485**(7400), 611–614 (2012).

#306820 https://doi.org/10.1364/OE.25.029098
Journal © 2017 Received 11 Sep 2017; revised 1 Nov 2017; accepted 1 Nov 2017; published 8 Nov 2017

Optics EXPRESS

10. T. Steinmetz, T. Wilken, C. Araujo-Hauck, R. Holzwarth, T. W. Hänsch, L. Pasquini, A. Manescau, S. D'Odorico, M. T. Murphy, T. Kentischer, W. Schmidt, and T. Udem, "Laser Frequency Combs for Astronomical Observations," Science **321**(5894), 1335–1337 (2008).
11. C. Xu and F. W. Wise, "Recent advances in fibre lasers for nonlinear microscopy," Nat. Photonics **7**(11), 875–882 (2013).
12. N. G. Horton, K. Wang, D. Kobat, C. G. Clark, F. W. Wise, C. B. Schaffer, and C. Xu, "In vivo three-photon microscopy of subcortical structures within an intact mouse brain," Nat. Photonics **7**(3), 205–209 (2013).
13. C. W. Freudiger, W. Yang, G. R. Holtom, N. Peyghambarian, X. S. Xie, and K. Q. Kieu, "Stimulated Raman scattering microscopy with a robust fibre laser source," Nat. Photonics **8**(2), 153–159 (2014).
14. J. M. Dudley, G. Genty, and S. Coen, "Supercontinuum generation in photonic crystal fiber," Rev. Mod. Phys. **78**(4), 1135–1184 (2006).
15. F. Leo, S. Coen, P. Kockaertl, S.-P. Gorza, P. Emplit, and M. Haelterman, "Temporal cavity solitons in one-dimensional kerr media as bits in an all-optical buffer," Nat. Photonics **4**(7), 471–476 (2010).
16. J. K. Jang, M. Erkintalo, S. G. Murdoch, and S. Coen, "Ultraweak long-range interactions of solitons observed over astronomical distances," Nat. Photonics **7**(8), 657–663 (2013).
17. F. Amrani, A. Haboucha, M. Salhi, H. Leblond, A. Komarov, P. Grelu, and F. Sanchez, "Passively mode-locked erbium-doped double-clad fiber laser operating at the 322nd harmonic," Opt. Lett. **34**(14), 2120–2122 (2009).
18. P. Grelu and N. Akhmediev, "Dissipative solitons for mode-locked lasers," Nat. Photonics **6**(2), 84–92 (2012).
19. S. Chouli and P. Grelu, "Rains of solitons in a fiber laser," Opt. Express **17**(14), 11776–11781 (2009).
20. E. G. Turitsyna, S. V. Smirnov, S. Sugavanam, N. Tarasov, X. Shu, S. A. Babin, E. V. Podivilov, D. V. Churkin, G. Falkovich, and S. K. Turitsyn, "The laminar–turbulent transition in a fibre laser," Nat. Photonics **7**(10), 783–786 (2013).
21. D. V. Churkin, S. Sugavanam, N. Tarasov, S. Khorev, S. V. Smirnov, S. M. Kobtsev, and S. K. Turitsyn, "Stochasticity, periodicity and localized light structures in partially mode-locked fibre lasers," Nat. Commun. **6**, 7004 (2015).
22. U. Keller, K. J. Weingarten, F. X. Kärtner, D. Kopf, B. Braun, I. D. Jung, R. Fluck, C. Hönninger, N. Matuschek, and J. Aus der Au, "Semiconductor saturable absorber mirrors (SESAMs) for femtosecond to nanosecond pulse generation in solid-state lasers," IEEE J. Sel. Top. Quantum Electron. **2**(3), 435–453 (1996).
23. O. Okhotnikov, A. Grudinin, and M. Pessa, "Ultra-fast fibre laser systems based on SESAM technology: new horizons and applications," New J. Phys. **6**(1), 177 (2004).
24. D. R. Solli, C. Ropers, P. Koonath, and B. Jalali, "Optical rogue waves," Nature **450**(7172), 1054–1057 (2007).
25. J. M. Soto-Crespo, P. Grelu, and N. Akhmediev, "Dissipative rogue waves: Extreme pulses generated by passively mode-locked lasers," Phys. Rev. E Stat. Nonlin. Soft Matter Phys. **84**(1 Pt 2), 016604 (2011).
26. C. Lecaplain, P. Grelu, J. M. Soto-Crespo, and N. Akhmediev, "Dissipative rogue waves generated by chaotic pulse bunching in a mode-locked laser," Phys. Rev. Lett. **108**(23), 233901 (2012).
27. J. M. Dudley, F. Dias, M. Erkintalo, and G. Genty, "Instabilities, breathers and rogue waves in optics," Nat. Photonics **8**(10), 755–764 (2014).
28. D. Abraham, R. Nagar, V. Mikhelahsvili, and G. Eisenstein, "Transient dynamics in a selfstarting passively modelocked fiberbased soliton laser," Appl. Phys. Lett. **63**(21), 2857–2859 (1993).
29. H. Li, D. G. Ouzounov, and F. W. Wise, "Starting dynamics of dissipative-soliton fiber laser," Opt. Lett. **35**(14), 2403–2405 (2010).
30. N. Sarukura and Y. Ishida, "Pulse evolution dynamics of a femtosecond passively mode-locked Ti:sapphire laser," Opt. Lett. **17**(1), 61–63 (1992).
31. D. R. Solli, J. Chou, and B. Jalali, "Amplified wavelength–time transformation for real-time spectroscopy," Nat. Photonics **2**(1), 48–51 (2008).
32. K. Goda, K. K. Tsia, and B. Jalali, "Serial time-encoded amplified imaging for real-time observation of fast dynamic phenomena," Nature **458**(7242), 1145–1149 (2009).
33. K. Goda and B. Jalali, "Dispersive Fourier transformation for fast continuous single-shot measurements," Nat. Photonics **7**(2), 102–112 (2013).
34. B. Wetzel, A. Stefani, L. Larger, P. A. Lacourt, J. M. Merolla, T. Sylvestre, A. Kudlinski, A. Mussot, G. Genty, F. Dias, and J. M. Dudley, "Real-time full bandwidth measurement of spectral noise in supercontinuum generation," Sci. Rep. **2**, 882 (2012).
35. C. Lecaplain and Ph. Grelu, "Rogue waves among noiselike-pulse laser emission: An experimental investigation," Phys. Rev. A **90**(1), 013805 (2014).
36. A. F. J. Runge, C. Aguergaray, N. G. R. Broderick, and M. Erkintalo, "Raman rogue waves in a partially mode-locked fiber laser," Opt. Lett. **39**(2), 319–322 (2014).
37. A. F. J. Runge, N. G. R. Broderick, and M. Erkintalo, "Observation of soliton explosions in a passively mode-locked fiber laser," Optica **2**(1), 36–39 (2015).
38. M. Liu, A. P. Luo, Y. R. Yan, S. Hu, Y. C. Liu, H. Cui, Z. C. Luo, and W. C. Xu, "Successive soliton explosions in an ultrafast fiber laser," Opt. Lett. **41**(6), 1181–1184 (2016).
39. G. Herink, B. Jalali, C. Ropers, and D. R. Solli, "Resolving the build-up of femtosecond mode-locking with single-shot spectroscopy at 90 MHz frame rate," Nat. Photonics **10**(5), 321–326 (2016).
40. G. Herink, F. Kurtz, B. Jalali, D. R. Solli, and C. Ropers, "Real-time spectral interferometry probes the internal dynamics of femtosecond soliton molecules," Science **356**(6333), 50–54 (2017).

Optics EXPRESS

41. S. Sugavanam, S. Fabbri, S. T. Le, I. Lobach, S. Kablukov, S. Khorev, and D. Churkin, "Real-time high-resolution heterodyne-based measurements of spectral dynamics in fibre lasers," Sci. Rep. **6**, 23152 (2016).
42. B. Kolner, "Space-time duality and the theory of temporal imaging," IEEE J. Quantum Electron. **30**(8), 1951–1963 (1994).
43. C. Zhang, J. Xu, P. C. Chui, and K. K. Y. Wong, "Parametric spectro-temporal analyzer (PASTA) for real-time optical spectrum observation," Sci. Rep. **3**, 2064 (2013).
44. Y. Yu, B. Li, X. Wei, Y. Xu, K. K. M. Tsia, and K. K. Y. Wong, "Spectral-temporal dynamics of multipulse mode-locking," Appl. Phys. Lett. **110**, 201107 (2017).
45. J. Goodberlet, J. Wang, J. G. Fujimoto, and P. A. Schulz, "Starting dynamics of additive-pulse mode locking in the Ti:A12O3 laser," Opt. Lett. **15**(22), 1300–1302 (1990).
46. F. Krausz, M. E. Fermann, T. Brabec, P. F. Curley, M. Hofer, M. H. Ober, C. Spielmann, E. Wintner, and A. J. Schmidt, "Femtosecond Solid-State Lasers," IEEE J. Quantum Electron. **28**(10), 2097–2122 (1992).
47. B. Vodonos, A. Bekker, V. Smulakovsky, A. Gordon, O. Gat, N. K. Berger, and B. Fischer, "Experimental study of the stochastic nature of the pulsation self-starting process in passive mode locking," Opt. Lett. **30**(20), 2787–2789 (2005).
48. H. A. Haus, E. P. Ippen, and K. Tamura, "Additive-pulse mode-locking in fiber lasers," IEEE J. Quantum Electron. **30**(1), 200–208 (1994).
49. F. X. Kärtner, I. D. Jung, and U. Keller, "Soliton Mode-Locking with Saturable Absorbers," IEEE J. Sel. Top. Quantum Electron. **2**(3), 540–556 (1996).
50. D. J. Richardson, R. I. Laming, D. N. Payne, V. J. Matsas, and M. W. Phillips, "Pulse repetition rates in passive, selfstarting, femtosecond soliton fibre laser," Electron. Lett. **27**(16), 1451–1453 (1991).
51. S. M. Kelly, "Characteristic sideband instability of periodically amplified average soliton," Electron. Lett. **28**(8), 806–807 (1992).
52. P. Ryczkowski, M. Närhi, C. Billet, J.-M. Merolla, G. Genty, J. M. Dudley, "Real-time measurements of dissipative solitons in a mode-locked fiber laser," https://arXiv:1706.08571 (2017).
53. D. Y. Tang, L. M. Zhao, B. Zhao, and A. Q. Liu, "Mechanism of multisoliton formation and soliton energy quantization in passively mode-locked fiber lasers," Phys. Rev. A **72**(4), 043816 (2005).
54. N. Akhmediev and M. Karlsson, "Cherenkov radiation emitted by solitons in optical fibers," Phys. Rev. A **51**(3), 2602–2607 (1995).
55. N. Y. Joly, J. Nold, W. Chang, P. Hölzer, A. Nazarkin, G. K. L. Wong, F. Biancalana, and P. S. J. Russell, "Bright spatially coherent wavelength-tunable deep-UV laser source using an Ar-filled photonic crystal fiber," Phys. Rev. Lett. **106**(20), 203901 (2011).
56. M. Erkintalo, Y. Q. Xu, S. G. Murdoch, J. M. Dudley, and G. Genty, "Cascaded Phase Matching and Nonlinear Symmetry Breaking in Fiber Frequency Combs," Phys. Rev. Lett. **109**(22), 223904 (2012).
57. K. E. Webb, Y. Q. Xu, M. Erkintalo, and S. G. Murdoch, "Generalized dispersive wave emission in nonlinear fiber optics," Opt. Lett. **38**(2), 151–153 (2013).
58. A. Mussot, A. Kudlinski, M. Kolobov, E. Louvergneaux, M. Douay, and M. Taki, "Observation of extreme temporal events in CW-pumped supercontinuum," Opt. Express **17**(19), 17010–17015 (2009).
59. A. V. Avdokhin, S. V. Popov, and J. R. Taylor, "Continuous-wave, high-power, Raman continuum generation in holey fibers," Opt. Lett. **28**(15), 1353–1355 (2003).
60. A. Kudlinski and A. Mussot, "Visible cw-pumped supercontinuum," Opt. Lett. **33**(20), 2407–2409 (2008).
61. G. B. Whitham, "Non-linear dispersive waves," Proc. R. Soc. 283(1393), 238–261 (1965).
62. Y. S. Kivshar and B. Luther-Davies, "Dark optical solitons: Physics and applications," Phys. Rep. **298**(2), 81–197 (1998).
63. F. Coppinger, A. S. Bhushan, and B. Jalali, "Photonic time stretch and its application to analog-to-digital conversion," IEEE Trans. Microw. Theory Tech. **47**(7), 1309–1314 (1999).
64. G. P. Agrawal, Nonlinear Fiber Optics (Academic, 2001), 203–209.
65. K. Goda, D. R. Solli, K. K. Tsia, and B. Jalali, "Theory of amplified dispersive Fourier transformation," Phys. Rev. A **80**(4), 043821 (2009).

1. Introduction

Advanced laser technologies, such as miniature design [1], scalable energy [2,3] and flexible wavelength [4,5], have empowered abundant advancements in optical communication [6], material processing [7,8], astronomical exploration [9,10], biological imaging [11–13], and even interdisciplinary studies. On the other hand, the bright laser beam, particularly when propagating in well-confined optical fibers with few-micron (μm) core sizes [14], can stimulate intriguing and fruitful nonlinear physics, e.g., Kerr cavity soliton generation [15], ultraweak soliton interaction [16], soliton pairing [17,18] and stochastic dynamics [19–21], which has vastly expedited the understanding of nonlinear physics problems spanning over a broad spectrum of disciplines. In extreme cases, furthermore, weak perturbations to the optical oscillators can produce drastic outbursts, e.g., intensive Q-switched mode-locking [22,23] and optical rogue wave (also known as killer wave in oceanography) [24–27]. These

Optics EXPRESS

unpredictable nonlinear shocks against the normal operation impede the progress on approaching ultimate performances, and even become a safety issue for some highly-stable environment such as clinical applications. Since those nonlinear phenomena are mostly ultrafast transients, it is essential to fully visualize and diagnose these evolving nonlinear events through time-resolved and continuous acquisition in complementary time and spectral domains. However, it is a historical problem that, the conventional characterization tools have long been limited by either insufficient spectral frame rate (e.g., CCD/CMOS-based spectrometers) or short record length (e.g., burst-mode streak camera) [28–30]. Apparently, a real-time high-resolution spectro-temporal analyzer operating in a continuous mode is yet to be demonstrated for better understanding the nonlinear optical physics as well as optimizing the laser performances.

Photonic time-stretch through dispersive chirp has recently been demonstrated as a high-throughput single-shot spectral analyzer [31–33] and has greatly enriched researches on nonlinear physics, e.g., supercontinuum generation [34], optical rogue wave observation [24,35,36], soliton explosion [37,38], as well as mode-locking and soliton-molecule formation [39,40]. Despite its superior performance in fs-ps regime, typically for transform-limited short pulses, time-stretch spectroscope (TSS) is inadequate for CW/quasi-CW optical signal, see Appendix 1. Therefore, CW/quasi-CW components involved in transient laser dynamics are easily overlooked by TSS, resulting in incomplete spectral information, which is particularly true for those nonlinear events evolved from CW/quasi-CW. Herink et al. [39] have recently demonstrated the spectral buildup of fs pulse by using TSS. Although broadband spectral dynamics can be revealed for the mode-locking regime, the spectral details of initial quasi-CW fluctuations before successful mode-locking are not completely captured. Meanwhile, heterodyne-based high-speed spectral analyzer has also recently been proposed for ultrafast spectral characterization of quasi-CW optical signal [41]. Unfortunately, the working bandwidth is practically limited — sub-GHz, which subsequently confines the spectral characterization of broadband pulses. Apparently, prior works primarily focus on spectral dynamics in either broadband pulse or quasi-CW regimes, while a time-resolved spectro-temporal observation of both regimes can significantly broaden the horizon of nonlinear optical physics.

Here, we present a real-time optical spectro-temporal analyzer (ROSTA) working for both CW/quasi-CW and short pulse, which is capable of providing high resolutions in both time and spectral domains. In the time domain, ROSTA provides a temporal resolution of ~70 ps for intensity monitoring. In the spectral domain, it enables a temporal resolution of 10's ns (corresponding to a 10's-MHz frame rate), as well as spectral resolutions of 0.03 nm and 0.14 nm for CW/quasi-CW and short pulse, respectively. ROSTA essentially provides complementary information for better understanding on the nonlinear physics of transient dynamics from different domains. To exemplify its practical applications, ROSTA is particularly applied to visualize the onset of passive mode-locking, which evolves from quasi-CW to polychromatic mixture. Therein, interesting spectro-temporal phenomena are uniquely observed for gaining new insight into the complexity of passive mode-locking.

2. Working principle of ROSTA

Figure 1 is the overview of ROSTA, while its detailed implementation is covered in Appendix 2. It is a multi-core optical system that contains three synchronized optical channels. The input signal (i.e., ultrafast events) from optical sources is simultaneously diagnosed in both time and spectral domains respectively for intensity monitoring and spectral analysis. In the time domain, the intensity of input optical signal is directly received and converted to electrical signal by a highspeed photodiode (PD, 15 GHz), yielding a temporal resolution of about 70 ps, which can be further optimized to <10 ps by using state-of-the-art highspeed PDs (e.g., Finisar XPDV4121R). The electrical signal is subsequently

Optics EXPRESS

sampled by a highspeed multichannel digitizer (8-bit), which provides a record length up to 6.4 ms at a sampling rate of 40 GS/s for each channel.

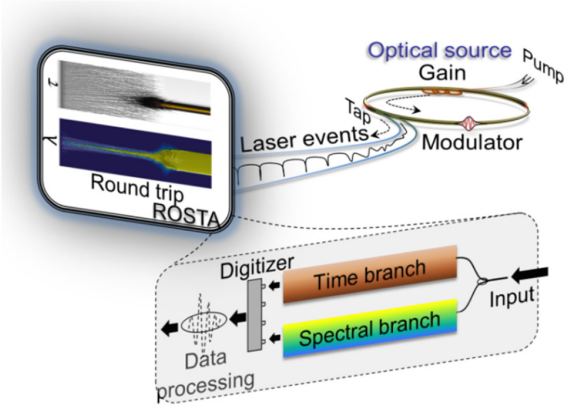

Fig. 1. The overview of ROSTA for ultrafast events observation. The ultrafast laser events from an optical source, i.e., a passively mode-locked fiber laser in this work, are launched into ROSTA through an optical splitter for spectro-temporal diagnosis.

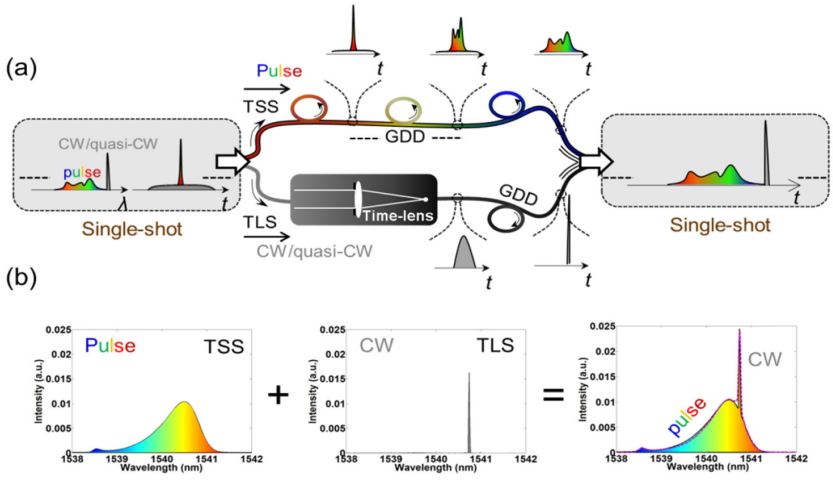

Fig. 2. (a) The schematic diagram of real-time spectroscope working for multiscale optical signals, ranging from CW to fs pulse. The ultrafast spectroscope of ROSTA has two sub-branches, i.e., TSS for pulse (upper) and TLS for CW/quasi-CW (lower), which respectively capture the spectral information of short pulse and CW/quasi-CW. TSS captures the spectral information of short pulse by time-stretching the input signal through a large GDD (–0.86 ns/nm), while TLS acquires the spectral information of CW/quasi-CW by temporal focusing. After data processing, see Appendix 4, a full picture of optical spectrum including both short pulse and CW/quasi-CW components is obtained in a single-shot manner. (b) An experimental illustration of single-shot spectroscopy for an optical signal with coexisting short pulse and CW components. Sub-figures from left to right are single-short spectra captured by TSS, TLS and their combination after data processing, respectively. The ensemble spectrum captured by a conventional OSA is also shown for comparison, i.e., the pink dashed curve.

In the spectral domain, the spectral information of input signal is captured in a single-shot manner by two complementary sub-channels respectively for short pulse and CW/quasi-CW components, see Fig. 2(a). The spectral information of short pulse is acquired through photonic TSS, i.e., the upper branch of Fig. 2(a). In brief, the short pulse is linearly chirped by a large group-delay dispersion (GDD), which arises from a wavelength-dependent propagation speed, $v_g = c / n_g(\lambda)$. As the group index $n_g(\lambda)$ is wavelength-dependent in

Optics EXPRESS

dispersive media, e.g., optical fibers in this work, the optical spectrum of a short pulse (transform-limited] can be mapped into the time coordinate, i.e., performing a single-shot wavelength-to-time transformation. TSS generates a linearly-chirped pulse waveform at a timescale ranging from ns to μs specifically determined by the amount of GDD, which is finally detected by another highspeed PD. The spectral resolution of present TSS is 0.14 nm, which is mainly defined by the amount of GDD [33] and can easily be improved to 10's pm by increasing the GDD. It should be emphasized that the frame rate (or temporal resolution) of TSS is intrinsically consistent with the occurrence rate of optical events, typically ranging from 10's to 100's MHz for standard laser cavities.

The spectral information of CW/quasi-CW components, on the other hand, is captured by a parametric time-lens spectroscope (TLS), the lower branch of Fig. 2(a). The ultrafast acquisition of TLS is enabled by the temporal imaging/focusing. A highspeed swept pump with linear chirp imparts temporal quadratic phase modulation to the input signal through parametric mixing, i.e., serving as a "time-lens" analogous to a spatial thin lens according to the space-time duality [42,43]. By incorporating output dispersion (GDD), a temporal two-focal-length (2*f*) system is constructed to perform optical Fourier transform — focusing different *optical* wavelengths into short pulses with different time delays. Assume a CW optical signal at a wavelength of λ, the optical field launched into the temporal 2*f* system can be expressed as

$$E_s = A\exp\left(i\frac{2\pi c}{\lambda}t\right), \tag{1}$$

where A is the amplitude of optical field. The time lens provides not only quadratic temporal phase modulation, but also a time gating owing to the finite temperature. Therefore, the optical field after the time lens can be expressed by

$$E_{time-lens} = E_s \cdot P(t) = \eta E_s \cdot rect\left(\frac{t}{T}\right)\exp\left(-i\frac{t^2}{2\Phi''_f}\right), \tag{2}$$

where $P(t)$ is the impulse response of time-lens. η, T and Φ''_f are the constant intensity coefficient, temporal aperture size and focal dispersion of time-lens, respectively. The output from time-lens is imparted by a linear chirp that can be compressed into a transform-limited pulse via the output dispersion, given by

$$E_{Output} = E_{time-lens} * C(t) = E_{time-lens} * \frac{1}{\sqrt{2\pi\Phi''_o i}}\exp\left(\frac{it^2}{2\Phi''_o}\right), \tag{3}$$

where $C(t)$ and Φ''_o are the impulse response and amount of output dispersion. * represents the convolution operation. Let $\Phi''_o = \Phi''_f$, the final output can be simplified to

$$E_{Output} = B\,\mathrm{Sin}\,c\left[\frac{T}{\Phi''_o}\left(t - \frac{2\pi c}{\lambda}\Phi''_o\right)\right], \tag{4}$$

where B includes the constant intensity and phase terms, see Appendix 3. Equation (4) clearly shows that, after passing through TLS, a CW input becomes a short pulse with a wavelength-dependent time delay, $\frac{2\pi c}{\lambda}\Phi''_o$. The spectral resolution of TLS is given by

$$\Delta\lambda_{TLS} = \frac{\Delta t\lambda^2}{2\pi c\Phi''_o}, \tag{5}$$

Optics EXPRESS

where Δt is the temporal resolution of detection system including PD and digitizer. In current work, TLS is realized by using swept-pump four-wave mixing (FWM) for temporal quadratic phase modulation, and an output GDD from a dispersive fiber for pulse compression. The spectral resolution of current TLS is 0.03 nm, see Appendix 2, while its frame rate is ~90 MHz. A higher frame rate can easily be obtained by correspondingly increasing the sweep rate of the swept pump used in FWM.

Finally, the real-time spectral information of both short pulse and CW/quasi-CW components respectively from TSS and TLS channels is reconstructed into a complete optical spectrum of input signal through precise data processing, and details have been covered in Appendix 4. Figure 2(b) showcases the single-shot ROSTA spectroscopy of an optical signal containing both short pulse and CW components. It is clear that the optical spectra of short pulse and CW components respectively captured by TSS and TLS are complementary to each other for full spectral information, which matches well with the ensemble version acquired by a standard optical spectral analyzer (OSA).

3. Studies of polychromatic transients involved in passive mode-locking

Apparently, ROSTA is appealing for the real-time diagnosis of multiscale optical signals. In particular, the birth of passive mode-locking usually experiences several distinguished regimes, typically from noise burst to quasi-CW, Q-switching and continuous mode-locking. Subject to specific cavity settings, e.g., pump intensity, cavity loss, polarization state, operating bandwidth, to name a few, hybrid combination of those polychromatic components can exist in a free-running passively mode-locked laser [22]. Although it has long been known in the laser community, the spectro-temporal observation of complex dynamics in passive mode-locking has been largely limited by conventional characterization tools in the past, which however is essential to better understand the physics behind [39]. Here, we employ ROSTA to observe the polychromatic transients involved in passive mode-locking, and some interesting features/phenomena are observed during the birth of mode-locking, which might have been overlooked by conventional characterization tools.

The mode-locked laser being investigated is a passively mode-locked fiber laser operating at 1.5 μm, which is similar with that of our prior work [44]. A fiber-based optical integrated module (OIM) with multiple functions, i.e., wavelength-division multiplexing (WDM), signal extraction, polarization selection and unidirectional operation, is used to loop the fiber ring cavity, which has a repetition rate of 34.2 MHz. The state of polarization (SOP) of lightwave is manipulated by an in-line polarization controller (PC) (Thorlabs PLC-900). Here, OIM and PC work together to form an artificial mode-locker, i.e., realizing the well-known nonlinear polarization rotation (NPR). The gain medium is a piece of erbium-doped fiber (EDF, Thorlabs ER80-8/125), 0.6 m in length. It is pumped through the OIM by a 980-nm laser diode (II-VI LC96AA74P-20), which has a maximum power of 600 mW. The lasing wavelength of fiber laser is tuned by a bandpass filter (BPF). The NPR mode-locking of this fiber cavity can be self-started by simply increasing the pump power beyond 80 mW. The emission of the fiber laser is controlled by using a fast chopper.

The reconstructed temporal and spectral evolutions of mode-locking process captured by ROSTA are illustrated in Fig. 3. At the early stage, the emission of laser cavity is weakly fluctuated as a quasi-CW centered at around 1540.8 nm, as shown in Fig. 4(ai), which lasts for about 1.2 ms. In the time domain, the noise burst occurs every ~21 ms, i.e., Fig. 4(bi), and corresponding fluctuations are also shown in the spectral domain, see Fig. 4(ai), i.e., a periodic intensity modulation on the narrowband spectrum. Inside the noise burst, there also are uprising noise pulses following the round-trip time of laser cavity (T_{rt}, ~34 ns in this case), as shown in the close-up of Fig. 4(bi). Those relatively-intensive noise pulses can arise from mode-beating between coexisting longitudinal modes with random phases, i.e., a quasi-CW state [45,46]. They actually provide seed pulses from which self-started mode-locking can evolve. It is because a particular intensive seed pulse can experience an increasing net

Optics EXPRESS

gain through the saturable-absorber nonlinearity as it circulates inside the laser cavity. This sustains until successful phase-locking between coexisting longitudinal modes is globally obtained, which yields a sharp and stable pulse. The remaining parts of incipiently-accompanied components, on the other hand, usually experience a negative net gain and thus eventually are suppressed, due to the gain competition in a homogenous gain medium, to be illustrated later. Interestingly, multiple noise pulses standing above the fluctuated background exist in the same round trip, while the pattern varies from burst to burst. It essentially implies the stochastic nature of a self-started mode-locking process, in which the stochastic seed pulses activate a pulse escaping over the entropic barrier [47].

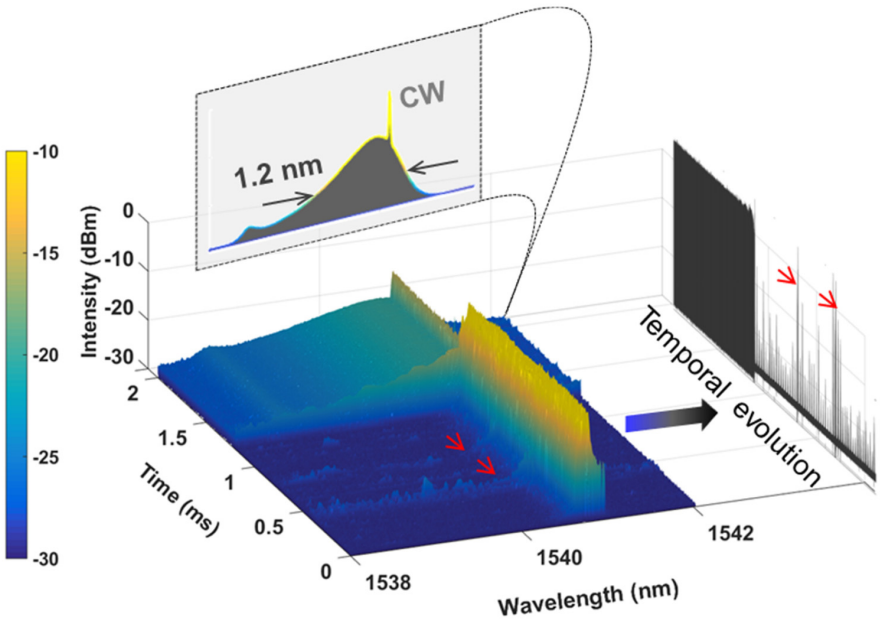

Fig. 3. The spatial-spectral evolution on the left side and the temporal evolution on the right side. Top inset shows a single-shot optical spectrum at the stable mode-locking stage.

Optics EXPRESS

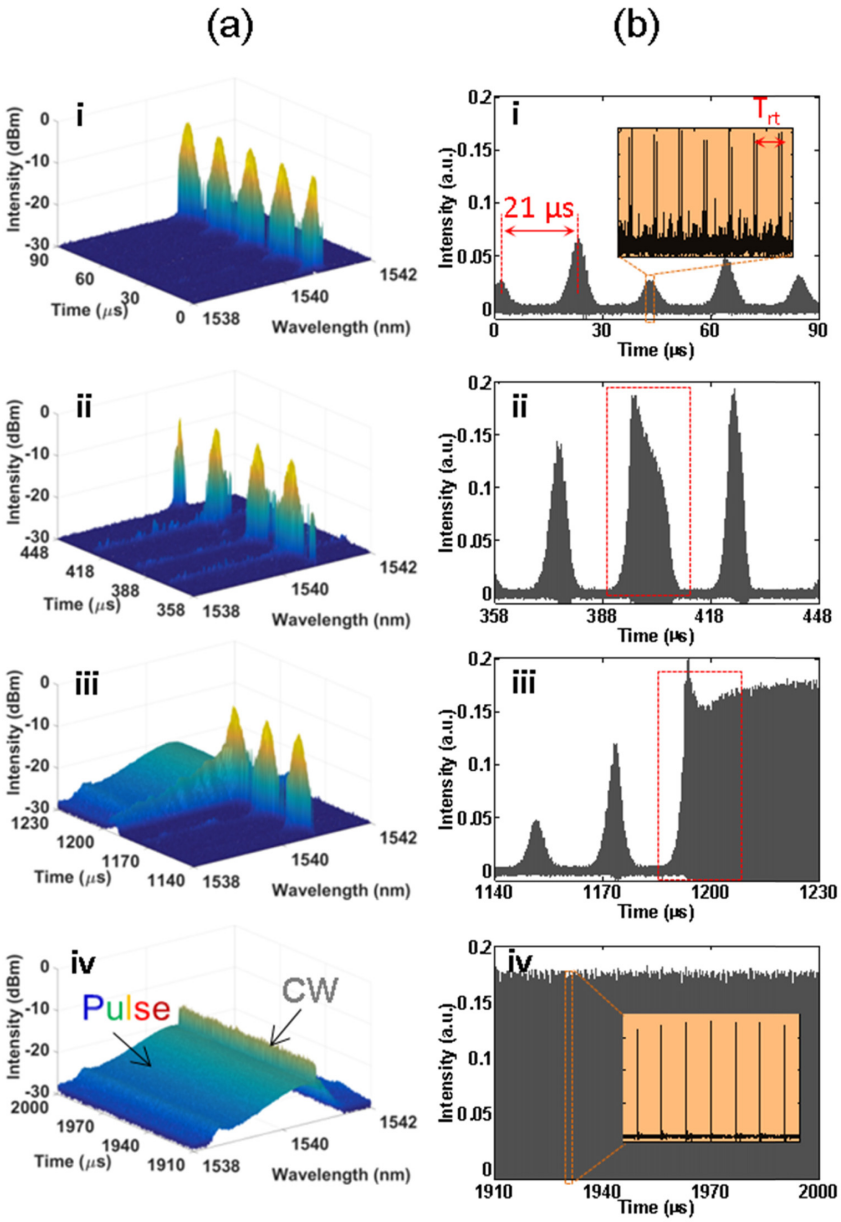

Fig. 4. The close-ups at different stages in both spectral (a) and time (b) domains, respectively. The birth of mode-locking experiences several stages, e.g., weak noise burst (ai, bi), strong shock (aii, bii), transition from fluctuation to mode-locking (aiii, biii), and finally stable mode-locking with coexisting CW component (aiv, biv). The red arrows indicate the strong shocks before successful mode-locking.

At about 0.4 and 0.8 ms, as indicated by the red arrows in Fig. 3, strong optical shocks appear in both time and spectral domains. It exhibits significant spectrum broadening in the spectral domain, as shown in Fig. 4(aii), while in the time domain, it delivers strong Q-switched-like noise bursts with envelopes almost four times higher than those at the early stage, as shown in Fig. 4(bii). In response to these strong optical shocks, it is likely to onset a mode-locking but fail (red dashed square in Fig. 4(bii)), while a successful case will be discussed later. This is because mode-locking can typically be obtained under a strong optical

Optics EXPRESS

shock [29], and the self-started mode-locking can be regarded as a trial-until-success process. At the appearance of intensive seed pulses from any origins, the laser emission tries to evolve into mode-locked pulse, before which it experiences many unsuccessful attempts. As such, the startup time of mode-locking is case sensitive, or even stochastic, for which reason a long record length provided by the spectro-temporal analyzer is essential for capturing the whole process.

Another Q-switched-like strong shock appears at about 1.2 ms, see Fig. 4(biii). Different from previous two cases at about 0.4 and 0.8 ms, its continuously-increasing intensity finally becomes stable in a short period of adjustment (about 20 μs), indicated by the red dashed square in Fig. 4(biii). Meanwhile, the peak intensity of short pulse following the round trip gradually increases until it is saturated. The generated pulse train shown in Fig. 4(biv) is much sharper than that at early fluctuated stage, as shown in Fig. 4(bi). An increasing peak intensity of circulating pulse, on the other side, implies a narrowing pulsewidth, since a sustaining pulse gets compressed in each round trip according to the mechanism of an effective mode-locker [48], until it is balanced by other factors, e.g., filtering and dispersion. This can also be verified by the gradually-broadening optical spectrum shown in Fig. 4(aiii), while a corresponding zooming-in 2D portrait is shown in Fig. 5(b). Particularly, the clean ground floor, as shown in the close-up of Fig. 4(biv), indicates a low-noise operation after mode-locking. The top inset of Fig. 3 illustrates a typical single-shot optical spectrum of mode-locked pulse. It has a spectral width of 1.2 nm at 3 dB, yielding a transform-limited pulsewidth of ~3.0 ps. More importantly, it is observed that at the mode-locking stage only a single pulse is circulating inside the laser cavity, although there are multiple seed pulses coexisting at the early stage.

In general, a buildup of passive mode-locking tends to evolve into a single-pulse operation while any other dispersive components would vanish, which is attributed to the nature of saturable absorbers, real or artificial ones [39,49]. In other words, accompanied CW/quasi-CW components are unlikely to appear in a passively mode-locked laser, or at least they have rarely been experimentally observed in the past. Here, we illustrate that the onset of mode-locking finally evolves into the coexistence of mode-locked short pulse and CW components, as indicated in Fig. 4(aiv). It is verified from the data processing that this sharp CW peak superimposed on the broad mode-locked spectrum is not shown in TSS but only in TLS, which confirms the non-pulse nature. Actually, this CW component is not presented in a short time interval right after mode-locking, i.e., 1200-1230 μs of Fig. 4(aiii). It has been newly generated at a wavelength almost the same as that of the quasi-CW at the early stage. It should also be emphasized that this accompanied CW peak is asymmetrically located on the right side of mode-locked spectrum, and it is different from those symmetrically-located discrete sidebands produced by either modulation instability (MI) [50] or periodic amplification [51], which have been widely observed in passively mode-locked fiber lasers. Although the wavelength of accompanied CW component is similar to that of the quasi-CW at the early stage, its intensity is weaker by ~7 dB, which can be attributed to the gain competition with mode-locked pulses. Interestingly, the mode-locked pulse train exhibits an additional intensity modulation in the time domain, at a period of ~0.5 μs as illustrated in Fig. 5(a). In response to this time-domain modulation, its optical spectrum evolves with spectral breathing, as indicated by the red dashed circle in Fig. 5(b). It can be attributed to the interaction between the accompanied components and mode-locked pulses, e.g., through cross-phase modulation (XPM) or FWM.

Optics EXPRESS

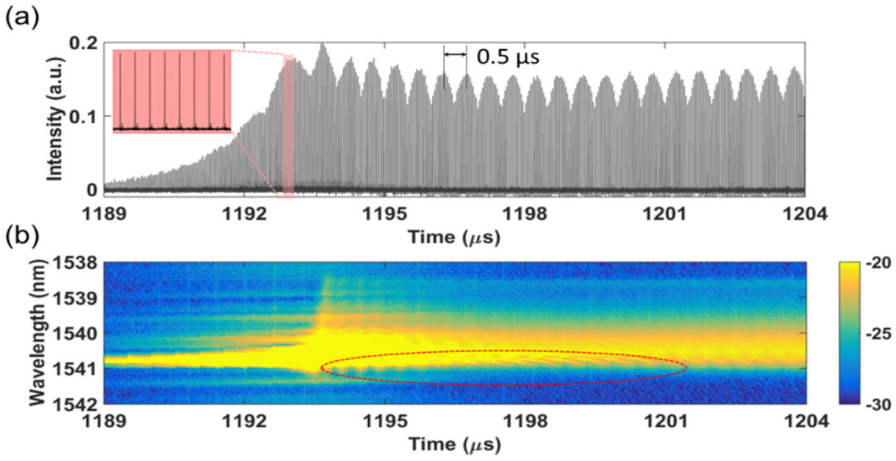

Fig. 5. (a) The intensity evolution in the transition from weak to strong pulses. Inset shows the close-up of pulse train repeated at the round-trip time of laser cavity, i.e., ~34 ns. (b) The corresponding spatial-spectral evolution in the spectral domain. The red dashed circle indicates the spectral breathing in response to the intensity modulation shown in a. Color bar represents intensity in log scale/

So far, self-started mode-locking has been successfully observed through ROSTA, and the coexistence of mode-locked pulse and CW components is sustained for subsequent operation. The combination of time-stretch and time-lens spectroscopies has complementarily enabled the spectro-temporal visualization of multi-scale spectral evolutions involved in the passive mode-locking, i.e., from quasi-CW to, short pulse and polychromatic mixture. It should also be mentioned that, as a complementary research, Ryczkowski et al. recently used time-lens as a high resolution real-time oscilloscope to observe the dissipative-soliton dynamics in a passively mode-locked laser [52]. The complementary effort and results significantly broaden the horizon of passive mode-locking that has been primarily investigated from conventional measurement systems. In our experiments, moreover, it is observed that the outcomes of different mode-locking onsets are sensitive to the setting of the fiber cavity, particularly the polarization state. We thus emphasize that the phenomena demonstrated above was observed in a specific setting of the fiber laser, which actually was an example of unusual cases. In some other rare cases, different spectro-temporal evolutions are also obtained, for example long birthing time, as shown in Fig. 6, and failure of mode-locking but with fruitful noise-pulse interactions.

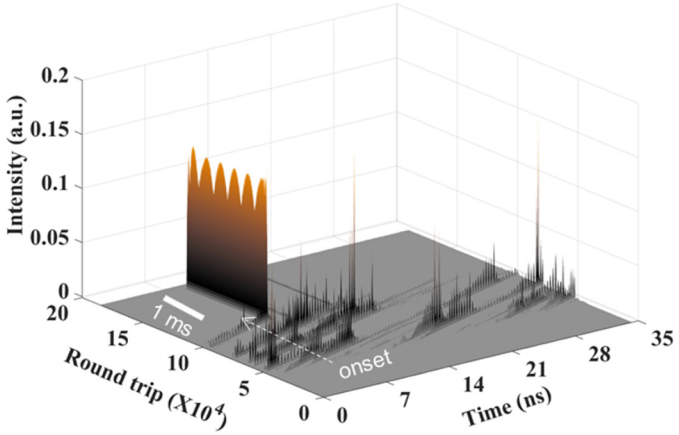

Fig. 6. The spatial-temporal evolution of mode-locking onset with a long birth time.

Optics EXPRESS

In the circumstance of polychromatic optical signal, the peak intensity of short pulse in the time domain can be orders of magnitude higher than that of CW component. In general, the polychromatic signal launched to PD for time-domain characterizations is properly attenuated to avoid optical saturation or signal distortion, particularly for intensive short pulses. As a result, the DC electrical signal generated by the CW component (if any) will be too weak and consequently immersed in the noise floor, given that the dynamic range of an analog-to-digital converter is typically limited to ~20 dB. In ROSTA, however, the intensity of coexisting CW component can be complementally recovered from the time-resolved spectra uniquely captured by TLS at a Nyquist rate equal to the frame rate of TLS, i.e., equivalent to an analog bandwidth that is half of TLS frame rate.

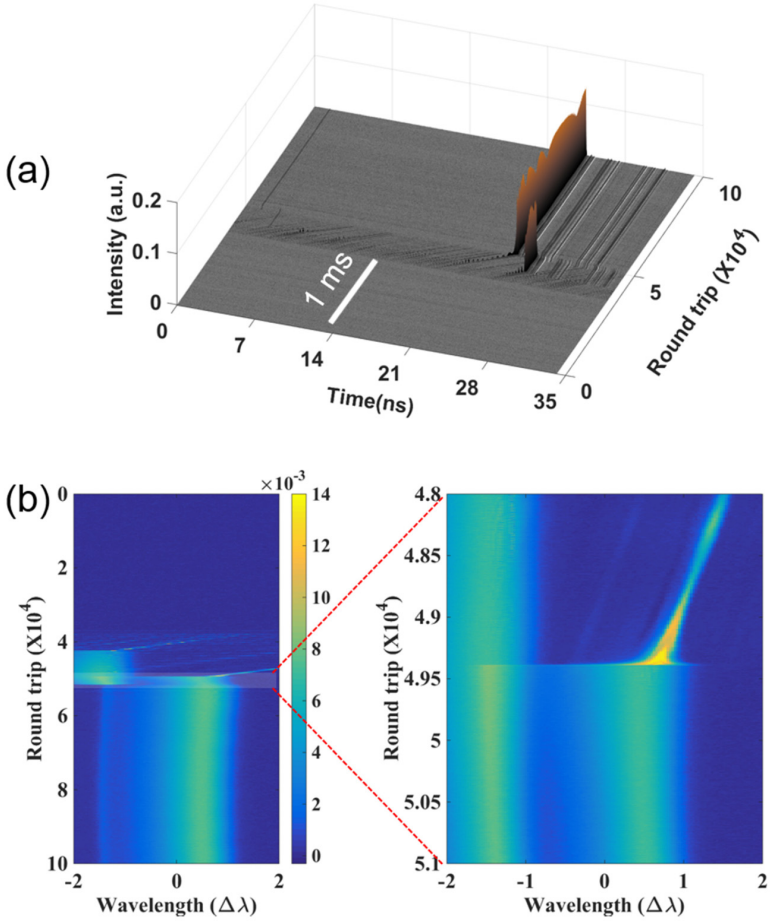

Fig. 7. The onset of mode-locking that results in pure pulse, i.e., without coexisting CW/quasi-CW components. (a) The spatial-temporal evolution. During the birth of mode-locking, there are two pulses successively raised up, but the first one loses the "competition" and vanishes right after the growth of the latter. (b) The corresponding spatial-spectral evolution. Color bar represents spectral intensity.

For practical applications, a mode-locked laser is usually required to operate in a continuous mode-locking regime without other perturbation components, e.g., dispersive and CW background. Indeed, we observe such kind of phenomenon in a certain setting of the fiber laser, and it can finally evolve into a pure mode-locking. Figure 7 illustrates an example that two pulses successively rise up at the early stage, but the first pulse vanishes soon after the growth of the second one. This phenomenon has rarely been experimentally unveiled

Optics EXPRESS

before. The mechanism behind it can be attributed to the fact that the second pulse obtains a preferential dominance from the saturable-absorber nonlinearity, as well as the laser cavity has insufficient gain to support two coexisting pulses owing to the energy quantization effect [53].

It is also noticed that the seed pulses at the early stage have a tilt angle on the spatio-temporal map, e.g., Fig. 7. It can be briefly explained as follows: the center wavelengths before and after mode-locking are different, as shown in Fig. 3, and the group velocities ($v_g = c / n_g(\lambda)$) in these two regimes are thus different, due to the wavelength-dependent group index $n_g(\lambda)$. It results in slightly different round-trip times for these two regimes, i.e., $T_{rt} = n_g(\lambda)L / c$, where L is the cavity length. In the data processing (Appendix 4), data stream sectioning is based on the round-trip time of well-established mode-locking regime, and therefore the regime before mode-locking is tilted.

4. Conclusion and discussion

We have demonstrated a multi-core real-time optical spectro-temporal analyzer for single-shot studies on nonlinear optical dynamics. It simultaneously provides temporal resolutions of ~70 ps in time domain and 10's ns (or 10's MHz frame rate) in the spectral domain, as well as a high spectral resolution for multiscale optical inputs, i.e., ranging from CW to fs pulses. Its non-trivial record length of up to 6.4 ms enables continuous observations of non-repetitive optical events over an extensive time period — equivalent to a propagation distance of ~1900 km. ROSTA has been applied to visualize the onset of passive mode-locking of a fiber laser, and interesting phenomena, e.g., evolution from quasi-CW noise burst to strong shock, transition from fluctuation to mode-locking, and coexistence of CW and mode-locked pulses, have been spectro-temporally observed in a single-shot manner for the first time.

The application of ROSTA is not confined to the spectro-temporal observation of polychromatic pulsations in mode-locked lasers as illustrated in this work. Many other applicable fields include: 1) a non-soliton pulse propagating in optical fibers can evolve into a soliton by shedding part of perturbed energy into a dispersive wave (DW, quasi-CW), which has played an important role in the wavelength conversion, particularly for the generation of deep-UV, visible or even mid-IR laser [54,55]. The fundamental physics of DW generation has traditionally been interpreted in the time domain as the coherent amplification (i.e., energy transformation) of a linear wave by an in-phase soliton propagating in the anomalous dispersion. However, a controversy has recently been raised that DW formation can generally be described in the spectral domain as the cascaded FWM process through phase-matching between CW components [56,57]. Consequently, extra efforts, particularly on the experimental investigation, are required for fully unsealing the essential mechanism of DW generation in the complementary time and spectral domains. To this end, the uniqueness of ROSTA is promising for observing and understanding the transient behaviors of DWs; 2) For the studies of interdisciplinary research problems, in addition, optical rogue wave has recently been proposed to understand the physics of killer wave in oceanography [24–27]. The characterization of optical rogue wave, however, has mostly been relied on ordinary wave-amplitude statistics, which largely prevents gaining insight into the mystery of its physical driving forces, e.g., how optical freak waves raise up from a quiet background, particularly when a CW pump is employed [58]. Similar problems also exist in the research field of CW-pumped supercontinuum generation [14,59,60]; 3) In fiber-optic systems, it is well known that a CW/quasi-CW radiation propagating in the anomalous dispersion can be broken up into a train of ultrashort pulses through the MI effect, which has been intensively studied since the 1960s for fluid dynamics, plasma physics as well as nonlinear optics [6,61]. In the spectral domain, MI process leads to two symmetrical sidebands, which is seeded by perturbations (e.g., spontaneous noise). Even though it is an old story, ultrafast spectro-temporal observations of breakup dynamics of CW/quasi-CW into ultrashort pulses during the MI

Optics EXPRESS

process has not been visualized yet, which is however significant for enlightening the impact of MI on a complex process involving other fruitful nonlinear effects, e.g., FWM, SPM, XPM, self-steepening and Raman scattering; 4) In contrast to the bright soliton, dark soliton manifests itself as a localized nonlinear wave (i.e., a hole) existing on a stable CW background [62], and it has evolved into a flourishing research area, for example vector dark solitons, dark and bright soliton pairs, ring dark solitons, parametric dark solitons, etc. Although the physics and stationary characteristics of dark soliton has been widely studied in the past, its nonlinear dynamics, e.g., the transient behavior of dark soliton formation and the interaction of dark solitons, or between dark and bright solitons, is scientifically interesting for better harnessing for practical applications. Therefore, it is believed that ROSTA will be a powerful tool for these areas mentioned before.

Appendix 1 — The limitation of time-stretch on quasi-CW inputs

The backbone of time-stretch process is the wavelength-dependent group velocity — group delay dispersion (GDD) [63]. In dispersive media, the group velocity v_g is a function of wavelengths due to a wavelength-dependent refraction index $n(\lambda)$, which thus can produce linear time delays for different wavelength components contained in a transform-limited pulse. Mathematically, the amount of dispersion in dispersive media is given by

$$GDD = \left(\frac{\partial \beta_1}{\partial \lambda}\right) \cdot L = -\frac{2\pi c}{\lambda^2} \beta_2 \cdot L, \tag{6}$$

where, β_1, β_2 and L are the group velocity, dispersion of group velocity and medium length, respectively. In time-stretch process, new frequency generation should be avoided; otherwise it delivers artificial spectral signal. As a consequence, nonlinear effects, which likely occur when the ultrashort pulse has a very high peak power (e.g., >kW), should be suppressed during the time-stretch. To this end, the optical signal launched to time-stretch spectroscope (TSS) should be properly attenuated. As such, it induces another issue — limited sensitivity, as a result of the optical loss from dispersive media, particularly when long optical fibers are used. Consequently, time-stretch favors dispersive media with a high ratio of dispersion to loss, e.g., the dispersion-compensating fiber (DCF) developing for optical communication.

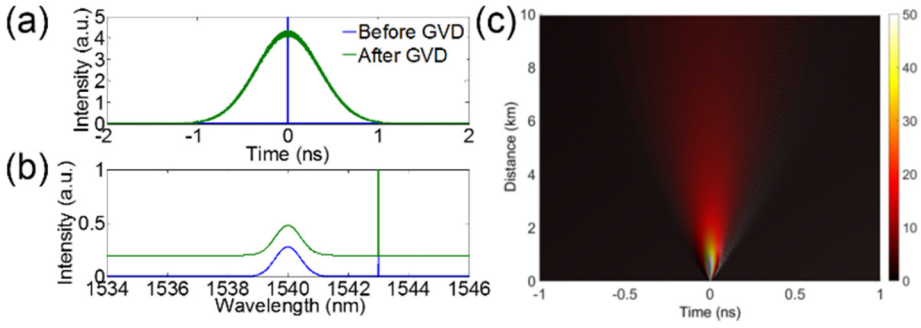

Fig. 8. (a) The time-domain waveforms before and after time-stretch via DCF. (b) The corresponding optical spectra. Noted that, optical spectra are vertically off-set for a better visualization, otherwise they are overlapped. (c) The spatio-temporal map of the pulse along the DCF. The β_2 used in this simulation is 0.1 ps^2/m, while the optical loss is not included in this simulation.

TSS can provide a superior performance for transform-limited ultrashort pulses, and has drawn intensive attention for high-throughput spectral diagnosis [33]. However, it has a non-

Optics EXPRESS

negligible weakness — only working for transform-limited short pulses, but not CW/quasi-CW. To illustrate this issue, numerical simulation is performed by solving the nonlinear Schrodinger equation (NLSE) through split-step Fourier method (SSFM) [64], as shown in Fig. 8. A transform-limited Gaussian pulse with a spectrum width of 1 nm centered at 1540 nm co-propagates with a 1543-nm CW through a dispersive medium, i.e., 10-km DCF. Figures 8(a) and (b) show the temporal and spectral waveforms before (blue) and after (green) the DCF. It is clear that the 1543-nm CW component is not shown on the time-stretched waveform. By zooming-in the ground of Fig. 8(a), it is recognized that the CW component has only contributed to the noise floor of time-stretch spectrum, rather than a sharp peak. Figure 8(c) illustrates the corresponding the spatio-temporal map, where the pulse is gradually broadened with a decreasing intensity.

This issue can also be experimentally verified, as shown in Fig. 9. The optical source used for this measurement is a mode-locked fiber laser with coexisting pulse and CW components, centered at 1557.8 nm and 1561.2 nm, respectively. The single-shot spectrum captured by TSS is illustrated in Fig. 9(b). As can be observed, the CW component has been vanished. As a consequence, a complementary single-shot spectroscope working for both short-pulse and CW/quasi-CW is essential.

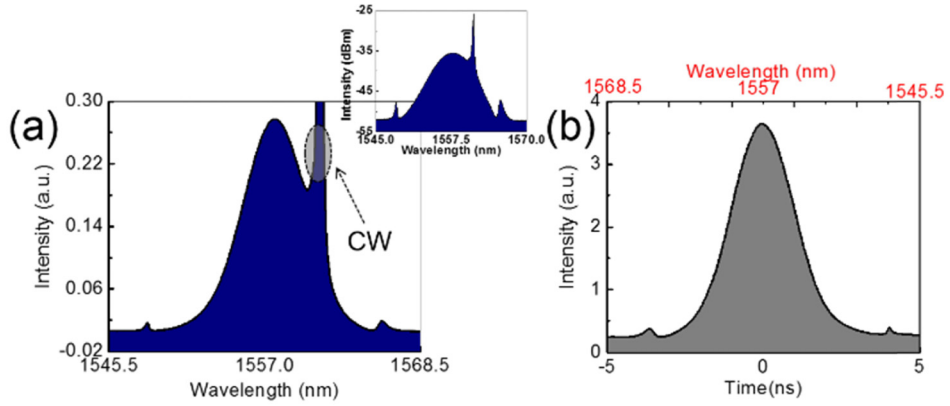

Fig. 9. (a) The optical spectra captured by a conventional OSA, where the CW peak is clearly shown. Inset shows the log-scale version. (b) The optical spectrum captured by TSS, where the CW peak has been unfortunately overlooked.

Appendix 2 — Experimental setup of ROSTA

The experimental setup of ROSTA is shown in Fig. 10(a). The optical signal is simultaneously diagnosed in three cooperative channels (i.e., multiple processing cores): spectral-domain channels TSS (channel 1) and TLS (channel 2), respectively for short-pulse and CW/quasi-CW components; time-domain channel Time (channel 3). In the TSS channel, the spectral information of short-pulse is captured by photonic time-stretch via GDD1, i.e., a DCF with a total dispersion of −0.85 ns/nm. The TSS output is detected by an 15-GHz photodetector (PD1, Agilent 11982A) and then sampled and digitized by a 4-channel real-time oscilloscope at a sampling rate of 40 GS/s (LeCroy SDA 820Zi-B). In the TLS channel, the spectral information of CW/quasi-CW is captured by three key parts, namely *time-lens*, *phase conjugation* and *output dispersion*. Time-lens is implemented by four-wave mixing (FWM) in a 150-m highly nonlinear dispersion-shifted fiber (HNL-DSF1), where the optical signal under test and swept pump interact through a parametric process. HNL-DSF1 has a nonlinear coefficient of 30 $W^{-1}km^{-1}$ and zero-dispersion wavelength (ZDW) of 1554.7 nm. The swept pump is generated by linearly chirping a mode-locked laser (MLL) through GDD3 (−3.92 ns/nm), which is then amplified to ~200 mW through two EDFAs. The swept pump pulse has a fundamental repetition rate of 89 MHz and a pulsewidth of 2 ns, which is served

Optics EXPRESS

as the incident aperture of time-lens. The idler generated in FWM1 is filtered out and amplified by an L-band EDFA before being launched into FWM2 for phase-conjugation. In FWM2, a CW pump at 1555.5 nm mixes with the amplified idler from FWM1 and converts it back to the original wavelength. After FWM2, the chirp direction of optical signal is opposite to that of swept pump of FWM1, to be shown in Fig. 11. The phase-conjugation signal is finally compressed to transform-limited pulse through the output dispersion GDD2. The TLS signal is detected by a 12.5-GHz PD (Newfocus 1544-B) and sent to real-time oscilloscope. In the Time channel, the optical signal is directly detected by a 32-GHz PD (HP 83440D). The time delays of these three channels due to different optical path lengths are measured before actual experiments, based on which the detected signals from different channels can be accordingly realigned and calibrated in the data processing.

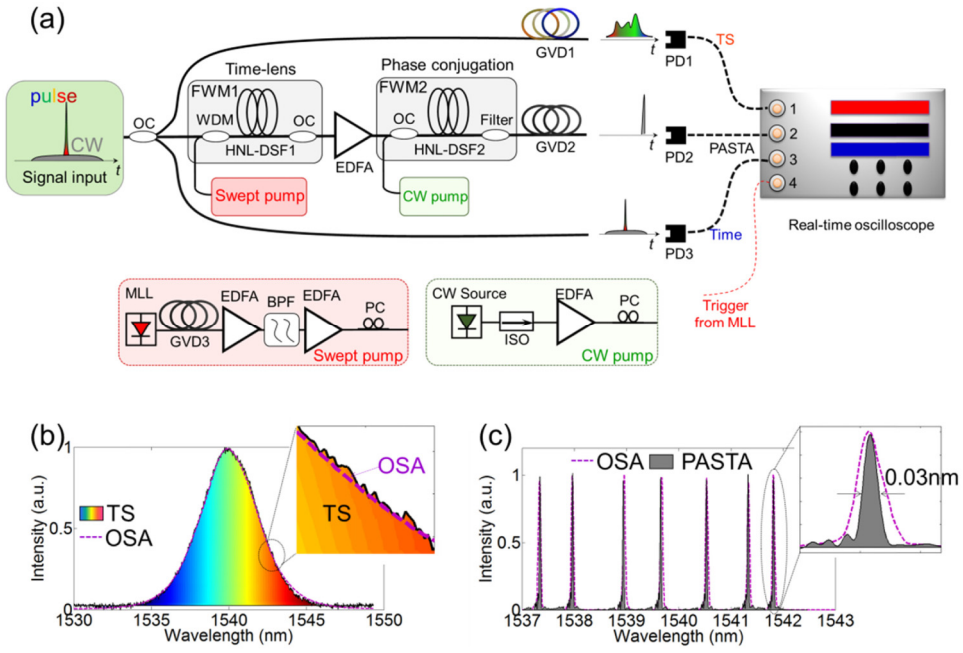

Fig. 10. (a) The overview of ROSTA implementation. (b,c) The basic performances of TSS and TLS, respectively. Here, the signal sources used for TSS and TLS measurement are a commercial mode-locked laser and multichannel CW laser, respectively. OC: optical coupler. FWM: four-wave mixing. PC: polarization controller. WDM: wavelength-division multiplexing. HNL-DSF: highly nonlinear dispersion-shifted fiber. GDD: group delay dispersion. EDFA: erbium-doped fiber amplifier. PD: photodiode. MLL: mode-locked laser. ISO: isolator. BPF: bandpass filter.

Appendix 3 — Principle of time-lens spectroscope (TLS)

In this section, we explain the principle of TLS through both theoretical derivation and numerical simulation, which will be performed by solving the NLSE using SSFM.

Based on the space-time duality [42], chromatic dispersion in dielectric media is analogous to the diffraction in free-space, and quadratic phase modulation in the time domain (named as time-lens) is functioned as that of a spatial thin lens. TLS is a temporal imaging system including time-lens and output dispersion, and it can also be regarded as a temporal *2f* system that focuses different wavelength components into short pulses at different time delays, i.e., effectively realizing a wavelength-to-time mapping. Therefore, the temporal waveforms output from TLS can provide spectral information of input optical signal.

Optics EXPRESS

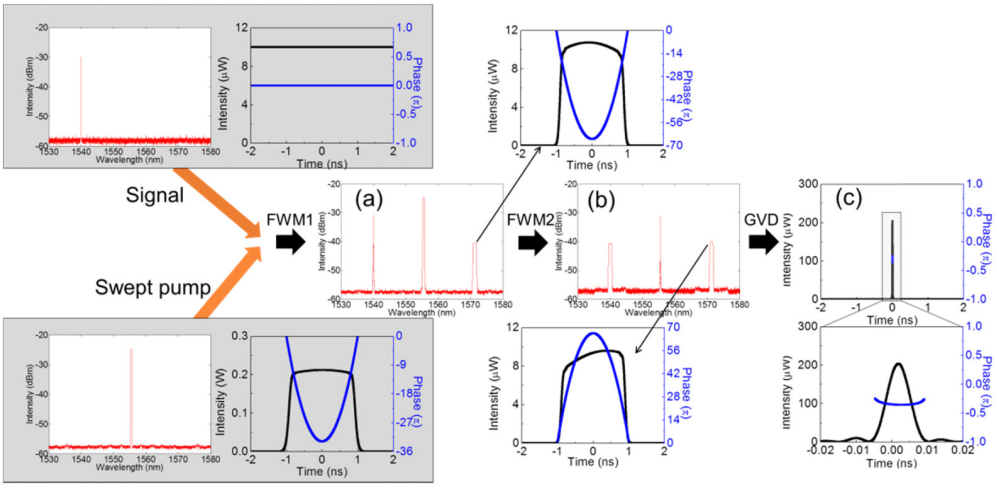

Fig. 11. (a) The output signal of FWM1. Top left inset shows the time- and spectral-domain waveforms of input signal, while the bottom left inset shows the swept pump. (b) The output signal of FWM2. (c) The result after pulse compression via output dispersion.

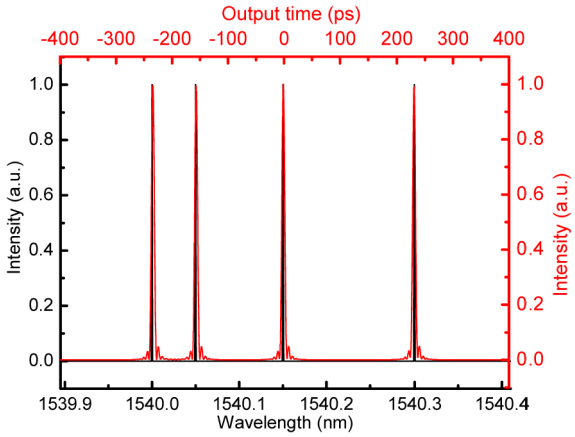

Fig. 12. The numerical result of TLS with a multiple-CW input.

TLS is implemented through two stages of FWMs, respectively for quadratic phase modulation (i.e. time-lens) and phase conjugation, see Figs. 9 and 10. For a CW input at a wavelength of λ_s, the optical field launched into FWM1 can be expressed as

$$E_s = A_s exp(i\frac{2\pi c}{\lambda_s}t), \tag{7}$$

where A_s is the amplitude. The output signal at the idler band of FWM1 is given by

$$F_{FWM1} = \eta_1 \cdot E_{p1}^2 \cdot E_s^*, \tag{8}$$

where η_1 is the conversion efficiency of FWM1, E_{p1} is the optical field of swept pump, which can be expressed as

$$E_{p1} = A_{p1} rect(\frac{t}{T}) exp(i\frac{2\pi c}{\lambda_p}t) exp(\frac{it^2}{2\Phi_p''}), \tag{9}$$

Optics EXPRESS

where A_{p1} and λ_p is the amplitude and center wavelength of swept pump, respectively. T is the incident aperture of time-lens (i.e., 2 ns in this study), which is defined by the duration of swept pump pulse generated by a dispersion of Φ''_p, i.e., GDD3 in Fig. 9(a). Thus, the output signal from FWM1 becomes

$$\begin{aligned} E_{FWM1} &= \eta_1 A_{p1}^2 A_s rect(\frac{t}{T}) exp[it(2\cdot\frac{2\pi c}{\lambda_p}-\frac{2\pi c}{\lambda_s})] exp(\frac{it^2}{\Phi''_p}), \\ &= A_{FWM1}\cdot rect(\frac{t}{T}) exp[it(2\cdot\frac{2\pi c}{\lambda_p}-\frac{2\pi c}{\lambda_s})] exp(\frac{it^2}{\Phi''_p}) \end{aligned} \tag{10}$$

where $A_{FWM1}=\eta_1 A_{p1}^2 A_s$ is the constant coefficient. Equation (10) shows that the input optical signal mixing with the swept pump generates a red-shifted idler with a quadratic phase modulation twice that of swept pump. In FWM2, the output signal from FWM1 is mixed with a CW pump centered at λ_p to perform phase conjugation, resulting in

$$E_{FWM2}=\eta_2\cdot E_{p2}^2\cdot E_{FWM1}^*, \tag{11}$$

Where η_2 is the conversion efficiency of FWM2, E_{p2} is the optical field of CW pump, given by

$$E_{p2}=A_{p2}\cdot exp(i\frac{2\pi c}{\lambda_p}t), \tag{12}$$

Adapting Eq. (10) and Eq. (12) into Eq. (11), we obtain

$$\begin{aligned} E_{FWM2} &= \eta_2 A_{p2}^2 A_{FWM1} rect(\frac{t}{T}) exp[it(2\cdot\frac{2\pi c}{\lambda_p}-2\cdot\frac{2\pi c}{\lambda_p}+\frac{2\pi c}{\lambda_s})] exp(-\frac{it^2}{\Phi''_p}), \\ &= A_{FWM2} rect(\frac{t}{T}) exp(i\frac{2\pi c}{\lambda_s}t) exp(-\frac{it^2}{\Phi''_p}) \end{aligned} \tag{13}$$

where $A_{FWM2}=\eta_2 A_{p2}^2 A_{FWM1}=\eta_1\eta_2 A_s A_{p1}^2 A_{p2}^2$ is the constant coefficient. From the analytical derivation, as well as the simulation results, to be shown later, it is shown that FWM2 not only inverses the quadratic phase of optical signal from FWM1, but also shifts the center wavelength back to the initial one. The effective function of those two FWMs is to introduce a temporal quadratic phase modulation without changing the center wavelength of input signal, i.e., served as a time-lens, and Eq. (13) can be simply expressed as

$$E_{time-lens}=E_{FWM2}=\eta E_s rect(\frac{t}{T}) exp(-i\frac{t^2}{2\Phi''_f}), \tag{14}$$

where $\eta=\eta_1\eta_2 A_{p1}^2 A_{p2}^2$ is the constant coefficient, and $\Phi''_f=\frac{1}{2}\Phi''_p$ represents the focal GDD of time-lens. It should be pointed out that, generally, FWM1 is already enough for quadratic phase modulation. Here, FWM2 is mainly used for reversing the quadratic phase of the output signal from FWM1, so that the same DCF can be utilized for subsequent pulse compression. Otherwise, the same amount of opposite dispersion provided by a long standard single-mode fiber (SMF), i.e., ~120 km, is required, which is lossy and thus largely reduces the sensitivity of TLS system.

Optics EXPRESS

The output signal from FWM2 is then compressed to a transform-limited pulse via output dispersion, given as

$$\begin{aligned} E_{Output} &= E_{time-lens} * C(t) = E_{time-lens} * \frac{1}{\sqrt{2\pi\Phi_o'' i}} exp(\frac{it^2}{2\Phi_o''}) \\ &= \eta \frac{1}{\sqrt{2\pi\Phi_o'' i}} exp(\frac{it^2}{2\Phi_o''}) \int_{-\infty}^{+\infty} E_s rect(\frac{t}{T}) exp(-i\tau^2(\frac{1}{2\Phi_f''} - \frac{1}{2\Phi_o''})) exp(-i\frac{t\tau}{2\Phi_o''}) d\tau \end{aligned} \quad (15)$$

where $C(t)$ and Φ_o'' represent the impulse response and dispersion amount of output dispersion, respectively, while * represents the convolution operation. Let $\Phi_o'' = \Phi_f''$, the expression can be simplified to

$$E_{Output} = A\int_{-\infty}^{+\infty} E_s rect(\frac{t}{T}) exp(-i\frac{t\tau}{2\Phi_o''}) d\tau = A'\mathcal{F}\left(E_s rect(\frac{t}{T}) \right)\Big|_{\frac{t}{\Phi_o''} - \frac{2\pi c}{\lambda_s}}, \quad (16)$$

where A and A' contain the constant intensity and phase terms. $\mathcal{F}$ is the Fourier transform operator. It is clear that TLS system performs optical Fourier transform on the time-gated input optical signal, i.e., mapping the spectrum into the time domain, and the final TLS output is given by

$$E_{Output} = B\,\mathrm{Sin}\,c(\frac{T}{\Phi_o''}(t - \frac{2\pi c}{\lambda_s}\Phi_o'')), \quad (17)$$

where B includes the constant intensity and phase term. It should be pointed out that only the intensity term can be detected by PDs in the actual measurements (see Fig. 9(c)). Thus, the intensity of B can be obtained through intensity calibration during data processing, to be discussed later. As a consequence, every CW signal passing through TLS will be interpreted as a short pulse with a wavelength-dependent time delay, $\frac{2\pi c}{\lambda}\Phi_o''$. The spectral resolution is given by

$$\Delta\lambda_{TLS} = \frac{\Delta t \lambda^2}{2\pi c \Phi_o''}, \quad (18)$$

where Δt is the temporal resolution of electrical detection system.

Numerical simulations is also performed for the TLS system, and shown in Fig. 11 (single input) and Fig. 12 (multiple inputs), which clearly show a wavelength-dependent time delay, i.e., wavelength-to-time mapping. While TSS enables single-shot spectral analysis for ultrashort transform-limited pulse, as discussed in Appendix 1, TLS system as a complement is much more suitable for CW/quasi-CW. Based on the temporal focusing mechanism, in addition, arbitrarily waveforms with relatively-long duration can also be detected by TLS, while the same wavelength components within the incident aperture will be focused onto the same time delay. Moreover, the input optical signal of TLS can experience an energy converging, and it actually is favorable for high detection sensitivity. On the other hand, TLS has its own limitations: the parametric FWMs' efficiency involved in TLS directly determines the system sensitivity. For an ultrashort pulse input ($\Delta\tau$, e.g. fs-ps), it has a very-limited interaction interval with the swept pump, i.e., $\frac{\Delta\tau}{T} < 0.001$. Therefore, the efficiency of FWMs in TLS system is expected to be very low for ultrashort-pulse inputs. This is also analogous to the case in free-space that a large spatial lens is hard to focus a very small optical beam.

Optics EXPRESS

Apparently, time-stretch and time-lens spectroscopies complement each other perfectly to perform spectral diagnosis for all kind of inputs, from CW/quasi-CW to ultrashort pulse.

Appendix 4 — Data processing

In ROSTA, spectral information is captured by two complementary single-shot spectroscopies — TSS and TLS, which of each obtains its best performance in the following way: TSS works for transform-limited short pulse, typically fs-ps; while TLS mainly searches for CW/quasi-CW spectral events. The heart of TSS is the linear chirp provided by dispersive media — GDD, i.e., −0.86 ns/nm in this case. It can spread out the wavelength components of an ultrashort pulse onto the time domain. The spectral resolution of TSS is defined by stationary phase approximation (SPA) [65], given by

$$\Delta\lambda_{TSS} = \lambda / sqrt(0.5 * C * GDD), \tag{19}$$

where λ is the center wavelength of optical pulse and C is the speed of light. In this work, a spectral resolution of 0.14 nm is obtained. Thus, TSS can only resolve the spectral features of a transform-limited short pulse with a spectral width wider than 0.14 nm, corresponding to a Gaussian pulse shorter than 26 ps. In the spectral domain, it results in a TSS waveform of $\Delta t_{TSS} = GDD * \Delta\lambda_{TSS} > 166\ ps$, which is much wider than the temporal resolution defined by the electrical bandwidth Δf (15 GHz in this case), i.e., $\Delta t_T = \frac{1}{\Delta f} = 67\ ps$. This actually defines a reference point for combining data from TSS and TLS channels to obtain a complete optical spectrum.

To accurately reconstruct the spectral and temporal evolutions of a laser dynamics, there are several important steps included in the data processing: 1) channel alignment; 2) wavelength and intensity calibration; 3) combining TSS and TLS for a full spectral dynamics.

A4.1 Channel alignment

ROSTA provides both time- and spectral-domain information of a laser dynamics through three cooperative channels, which however have different time delays due to different optical path lengths. As such, the same optical event simultaneously launched into these three channels will arrive the multichannel digitizer at different time delays, as shown in the inset of Fig. 13. Therefore, it is required to measure their time delays for subsequent data processing. To this end, a low-repetition-rate short pulse (ps at ~10 kHz) is used to measure the time delays of different channels. Based on this, the temporal traces of all three channels can be accurately aligned.

Optics EXPRESS

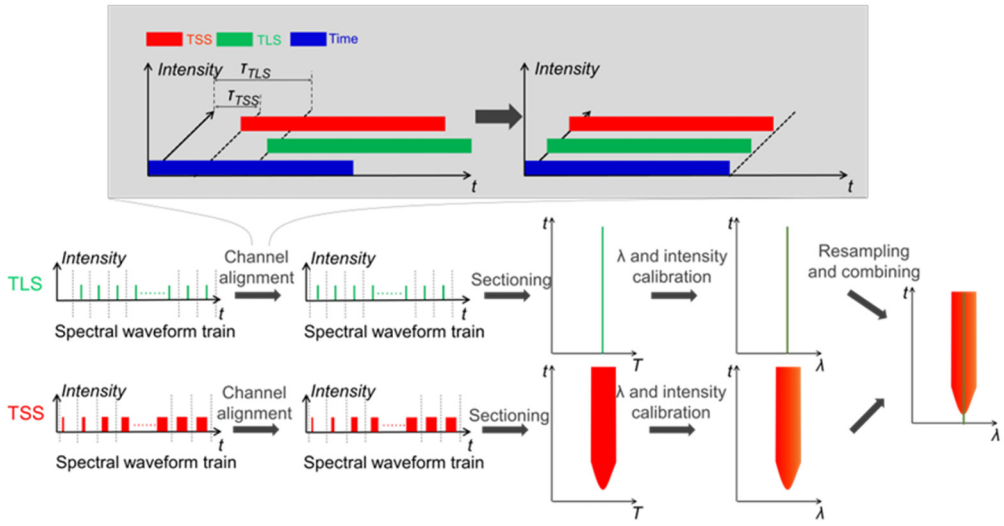

Fig. 13. The flow diagram of data processing. Inset sketches the time-domain data streams before and after channel alignment.

A4.2 Wavelength and intensity calibration

Since the temporal data streams from TSS and TLS channels by themselves have no wavelength coordinate, wavelength calibration should be performed for the consecutive temporal waveforms before correctly providing spectral information.

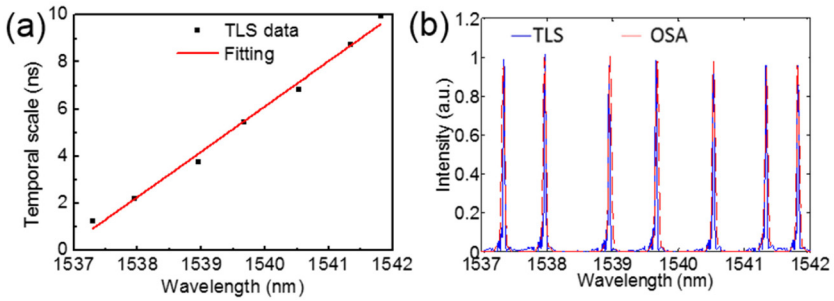

Fig. 14. (a) Wavelength-to-time mapping curve. (b) Calibrated TLS spectrum compared with that of OSA.

For the wavelength calibration of TLS, a 20-channel arrayed waveguide grating (AWG) with a channel spacing of 100-GHz (about 0.8 nm at 1.5 μm) is used to multiplex CW lasers, each of which has a linewidth of 50 kHz — far less than the spectral resolution of TLS. The multiplexed CW-signal is simultaneously measured by both standard OSA and TLS. By simply projecting the pulse waveform of TLS to that of OSA spectrum, a wavelength-to-time mapping curve can be obtained, as shown in Fig. 14(a), and the mapping ratio is calculated to be 1.92 ns/nm. After calibrating with this wavelength-to-time mapping curve, the TLS spectrum can horizontally (wavelength coordinate) match with the OSA spectrum, see Fig. 14(b). This mapping curve is primarily determined by the output dispersion of TLS and is fixed throughout all experiments, and thus it is single-calibration-for-ever. During experiments, in addition, there are two methods to expedite the data processing: i) the data acquisition of ROSTA system can be triggered by a time reference, provided by the MLL pump source of TLS; ii) a weak CW reference at 1537.5 nm, as a spectral mark, is launched together with the optical signal into TLS through a 90:10 fiber coupler, not shown in Fig.

Optics EXPRESS

10(a). As a result, the time reference, spectral mark and mapping ratio can effectively expedite the data processing.

For wavelength calibration of TSS, on the other hand, the mapping ratio from wavelength to time domains is given by the GDD used for pulse chirping, i.e., –0.86 ns/nm in this work. A good matching between TSS and OSA spectra is also obtained, as shown in Fig. 10(b). Given that TSS waveform train is always synchronized with its time-domain pulse train (channel 3), both time reference and spectral mark can be obtained from channel 3.

The spectrum intensity calibrations of TSS and TLS are performed in following way: a stable short-pulse laser with coexisting CW is captured by TSS, TLS and OSA. Both TSS and TLS spectra are averaged over 20 μs to match the case of conventional OSA working at average mode. The watt-to-voltage mapping ratios are obtained through comparing the voltages of both TSS and TLS spectra with the intensity of OSA spectrum, i.e., 76.3 μW/V and 2.0 mW/V for TSS and TLS, respectively, as shown in Fig. 15. While the absolute spectral intensity level can be affected by several factors, such as loss difference between different channels, nonlinear responsibility of PDs as well as the accumulation time of OSA, the relative intensity level at different spectral positions as well as different measurement frames are good enough for the general validation of the spectral dynamics studies.

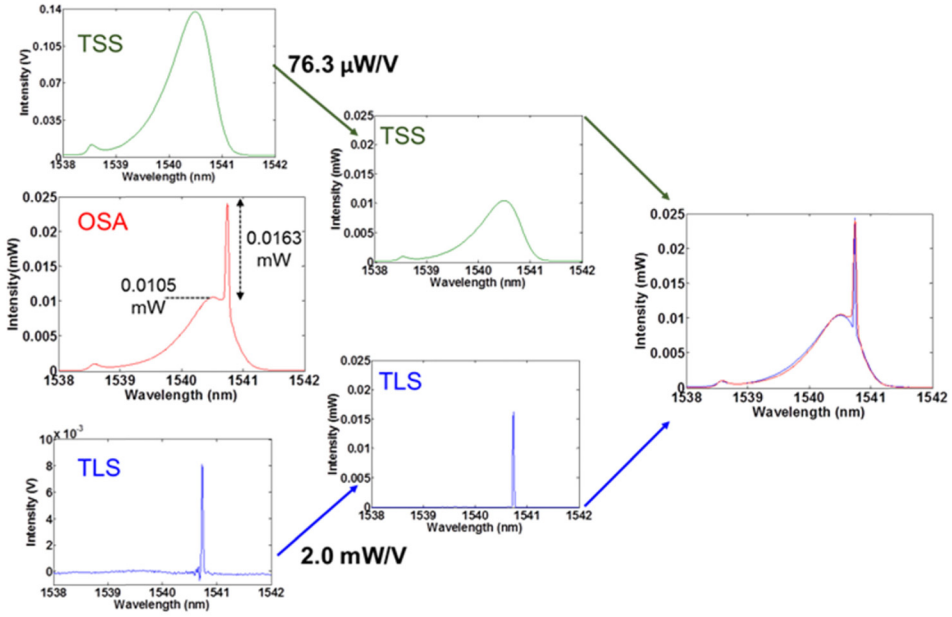

Fig. 15. Spectrum intensity calibration of ROSTA.

A4.3 Combining TSS and TLS

After obtaining the wavelength and intensity calibration information, the spectral information from TSS and TLS is ready for being combined for a full spectral evolution. Firstly, the one dimensional waveform trains of both TSS and TLS are sectioned into 2D matrixes, which can be subsequently lined up according to the propagation time, as shown in Fig. 13. The sectioning period of TSS and TLS is basically determined by their frame durations, i.e., the round-trip time of laser cavity under test for TSS, while the frame period of swept source (FWM1) for TLS. Then, wavelength and intensity calibrations are performed to those spectral segments based on what has been obtained before. It is noted that, since TSS and TLS have different frame rates and wavelength-to-time mapping ratios, their 2D spectral matrices have different sizes. In our data processing, three frames of the TLS matrix that temporally near the corresponding TSS frame are averaged into a new TLS frame, and thus a new data matrix of

Optics EXPRESS

TLS with the same size of TSS matrix is generated. Finally, the spectral matrices are simply added together on the criteria introduced at the beginning of this section.

Funding

Research Grants Council of the Hong Kong Special Administrative Region, China (Project Nos. HKU 17205215, HKU 17208414, and CityU T42-103/16-N); National Natural Science Foundation of China (N_HKU712/16); Innovation and Technology Fund (GHP/050/14GD); University Development Fund of HKU.